Interfacial engineering of Ni(OH)$_2$ on W$_2$C for remarkable alkaline hydrogen production

Hong Chuan Fu, Xiao Hu Wang, Xiao Hui Chen, Qing Zhang, Nian Bing Li [*], Hong Qun Luo [*]

School of Chemistry and Chemical Engineering, Southwest University, No. 2 Tiansheng Road, Beibei District, Chongqing 400715, People's Republic of China

A B S T R A C T

Promoting water dissociation kinetics and hydrogen desorption ability is the key challenge of tungsten carbides for boosting hydrogen evolution reaction (HER) in alkali environment. Here, we report that an interfacial engineered W$_2$C–Ni(OH)$_2$ electrocatalyst consisting of Ni(OH)$_2$ layer-encapsulated W$_2$C nanowire array can afford current densities of 10 and 100 mA cm^{-2} with overpotentials of only 60 and 213 mV in 1.0 M KOH, respectively, which not only surpasses the most previously reported W$_2$C-based examples, but even outperforms the commercial Pt/C catalyst at high current densities. The experimental results based on the classic bifunctional mechanism suggest that Ni(OH)$_2$ mainly acts as the scissors for the dissociation of water, and the W$_2$C site serves as the location for the adsorption and desorption of hydrogen. Further density functional theory calculations reveal that the hybridization of W$_2$C with Ni(OH)$_2$ can also alleviate the strong tungsten—hydrogen bond, further optimizing the hydrogen adsorption energy of the hybrid.

1. Introduction

Hydrogen is extensively hailed as an ideal candidate for highly polluting fossil fuels benefiting from its outstanding energy density and eco-friendly properties [1,2]. Among various approaches for industrial hydrogen production, hydrogen evolution reaction (HER) via water electrolysis is the most feasible benefiting from its suitable manufacturability [3]. Currently, alkaline HER dominates water electrolysis as it can produce high-purity hydrogen without corrosion damage and acid-mist contamination [4–7]. However, despite numerous attempts, it is still challenging to construct superior alkaline HER catalysts [8,9]. Platinum (Pt), as the benchmark HER catalyst, is difficult to be further applied because of its high cost, low abundance, and poor durability [2]. Thus, the intensive research on designing high-efficiency and enduring nonprecious electrocatalysts is in much demand.

Over the past years, tungsten carbide-based materials, e.g., W$_2$C and WC, have attracted wide interest in the HER field because of their analogous electronic structures with Pt [10–12]. Among them, W$_2$C exerts significantly better catalytic activity because of its much favorable hydrogen adsorption free energy (ΔG_{H*}) as demonstrated by previous theoretical calculations [12]. Despite its much less negative ΔG_{H*}, W$_2$C still binds relatively strongly to hydrogen intermediates, typical to tungsten carbides in general [12–14]. To further optimize ΔG_{H*}, very

recently, doping or hybridizing has been demonstrated to be effective to promote the hydrogen desorption on the surface of W$_2$C [10,13–18]. For example, Wang's group reported a twinned W$_2$C–WN hybrid to exhibit excellent HER performance, demonstrating that the N–W–C interface between W$_2$C and WN endows the W site with more favorable hydrogen desorption ability [17]. However, these researches have been exclusively focused on acidic HER, while researches on the alkaline HER catalysis of W$_2$C are far from enough. The main challenges can be understood in the following ways: (1) W$_2$C has a strong affinity with hydroxyl groups in alkaline media [14,19,20], which is likely to lead to a high energy barrier of water dissociation; (2) W$_2$C suffers from the corrosion damage in the strong alkaline media due to its metastable structure, which can result in the unsatisfactory long-term durability [14,18]; (3) for this carbon-deficient tungsten carbide, its further application is greatly hindered by lacking of reliable synthetic method [12,14,21].

From the perspective of catalyst design, it is a consensus that all strategies should aim to reduce the overall energy barrier regarding the reaction mechanism. However, the intrinsic mechanism for alkaline HER, unlike the well-documented acidic HER mechanism, remains controversial because of its multi-step reaction pathway. Despite several theories, e.g., hydrogen binding energy (HBE) theory [22–25], interface water and/or anion transfer theory [26,27], and bifunctional theory [7,

---

28], have been proposed, it should be admitted that the bifunctional theory is the most widely accepted as the catalyst design principle for alkaline HER in practice [29–34]. However, only ΔG_{H*} as the descriptor has been optimized in most of the currently reported W_2C-based catalysts in alkaline HER, and it remains unclear whether water dissociation can be accelerated. Therefore, creating additional water dissociation sites through interfacial engineering may be a feasible way to realize the optimal alkaline HER process for W_2C catalyst, and thus individual parts of the overall multi-step HER process can be accelerated by different constituents. Especially for the classic bifunctional system, "Ni(OH)$_2$–Pt", Ni(OH)$_2$ typically functions simply as an accelerator for water dissociation, whereas for H* consumption, it just serves as a "spectator" and hardly interacts with Pt [7,28]. However, for bi-component catalysts, the intimate contact at interfaces inevitably results in surface modification and electron redistribution, which can impact the ΔG_{H*} of H* consumption catalysts [35]. Therefore, we should be more rigorous to understand the extension of the bifunctional mechanism to more economic "Ni(OH)$_2$–Pt"-like hybrid catalysts.

Inspired by the above considerations, a hierarchical W_2C–Ni(OH)$_2$ array consisting of a crystalline W_2C core and an amorphous Ni(OH)$_2$ shell was fabricated through hydrothermal growth, carbonization, and electrodeposition operations. Benefiting from the intimate interfacial coupling and the strong electron interaction, the resulting hierarchical heterostructure exhibits remarkable alkaline HER catalytic activity. More inspiringly, W_2C–Ni(OH)$_2$ exhibits robust stability without any obvious current attenuation after multi-current stability testing. Further density functional theory (DFT) calculations verify that synergistic effects can be achieved at the interface between W_2C and Ni(OH)$_2$, giving rise to favorable hydroxyl and hydrogen species energetics on the hybrid surface. As a promoter for W_2C, the Ni(OH)$_2$ promotes water dissociation, meanwhile it accommodates the electrons from W_2C, which facilitates the hydrogen desorption at W sites. And the results reveal a crosslink of both bifunctional mechanism and HBE theory in the W_2C–Ni(OH)$_2$ hybrid system. Our work provides a potential interfacial engineering strategy for constructing efficient carbide-based HER catalysts in alkali.

2. Experimental section

2.1. Preparation of WO$_3$

In a typical process, 1.5 mmol of Na$_2$WO$_4$·2H$_2$O was dissolved in 20 mL of water and the pH value was adjusted to 1.2 with 3 M HCl. Then, 4.2 mmol of H$_2$C$_2$O$_4$ and 11.4 mmol of (NH$_4$)$_2$SO$_4$ were added, and the mixture was subsequently diluted to 30 mL. And the above uniform mixture containing 3 × 3 cm^2 carbon cloth (CC) sealed in a 50 mL Teflon-lined autoclave was heated at 180 °C for 12 h. Finally, the obtained WO$_3$ on CC was rinsed with distilled water and ethanol and dried at 60 °C for 12 h. The mass loading of WO$_3$ is about 14.5 mg cm^{-2}, and the calculated W loading is about 11.5 mg cm^{-2}.

2.2. Preparation of W$_2$C

A combustion boat containing a piece of WO$_3$ on CC (1 × 1 cm^2) and 0.3 g of melamine was calcined at 800 °C under Ar atmosphere for 2 h, and W$_2$C was then obtained. For comparison, WN and W were prepared at 700 and 900 °C, respectively. WO$_2$ was prepared similar to W$_2$C, except that the addition of melamine was reduced to 0.05 g.

2.3. Preparation of W$_2$C–Ni(OH)$_2$

The Ni(OH)$_2$ layer was coated on W$_2$C by electrodeposition operation, in which Pt foil and Ag/AgCl (3 M KCl) were utilized as the counter electrode and reference electrode; the W$_2$C acted as the working electrode; 0.1 M Ni(NO$_3$)$_2$ aqueous solution was utilized as the electrolyte. The chronopotentiometric method was carried out for 200 s at a cathodic current density of 5 mA cm^{-2}. Then, W$_2$C–Ni(OH)$_2$ was obtained. Ni(OH)$_2$ was prepared with the same electrodeposition condition except that bare carbon cloth instead of W$_2$C was used as the electrode. The loading of Ni(OH)$_2$ on W$_2$C nanowires is about 1 mg cm^{-2}.

3. Results and discussion

3.1. Electrocatalyst synthesis and characterization

Briefly, the W$_2$C–Ni(OH)$_2$ was fabricated by hydrothermal reaction, carbonization, and electrodeposition operations exhibited in Fig. 1. Firstly, uniformly distributed WO$_3$ arrays (named WO$_3$) are prepared on carbon cloth by the traditional hydrothermal process [36]. Then a high-temperature carbonization treatment was executed to trigger the phase transformation of WO$_3$ to W$_2$C. Finally, W$_2$C as the substrate was conducted for electrodeposition of W$_2$C–Ni(OH)$_2$.

The morphology of the various samples was revealed by scanning electron microscopy (SEM). Figs. 2a and S1 show WO$_3$ with typical nanowire-array morphology. After carbonization treatment, the overall array structure of W$_2$C has been well maintained (Figs. 2b and S2). After the electrodeposition of W$_2$C, a smooth plating layer can be observed on the surface of W$_2$C (Fig. 2c). And the obvious distribution of Ni together with W indicates the successful introduction of Ni domains (Fig. 2d). Fig. S3 shows the SEM and corresponding mapping images of the bare Ni(OH)$_2$, presenting a typical sheet-like structure. To get further structure details of the W$_2$C–Ni(OH)$_2$, transmission electron microscopy (TEM) studies were performed. As shown in Fig. 2e, f, the hierarchical Ni(OH)$_2$ layer can be observed at the edge of the nanowire. Further high-resolution TEM image confirms an amorphous state of the Ni(OH)$_2$ layer, and the well-resolved lattice fringe with the spacing of 0.23 nm is in good agreement with the (101) plane of W$_2$C (Fig. 2g). Moreover, the corresponding selected area electron diffraction (SAED) analysis further corroborates the crystalline structure of W$_2$C–Ni(OH)$_2$, and the diffraction rings match well with (002) and (101) planes of W$_2$C (Fig. 2h). And the uniform distribution of W and Ni in STEM-EDX images further confirms the core-shell structure (Fig. 2i).

The phase composition information of resultant catalysts was revealed by X-ray diffraction (XRD) patterns. The peak observed at 25.6° in all samples is associated with carbon cloth substrate. Fig. S4a shows the XRD pattern of WO$_3$ precursor. Fig. 3a shows the XRD patterns of W$_2$C, W$_2$C–Ni(OH)$_2$, and Ni(OH)$_2$. After carbonization treatment, the obtained W$_2$C has a good crystallinity, and the peaks at 34.5°, 38.0°, 39.6°, 52.3°, 61.9°, and 69.8° are in good agreement with the (100), (002), (101), (102), (110), and (103) planes of hexagonal W$_2$C (JCPDS No. 35-0776), respectively. After electrodeposition, new peaks in W$_2$C–Ni(OH)$_2$ can be barely detected, which further indicates that the newly introduced phase is amorphous. Similarly, there is also no obvious diffraction peak in Ni(OH)$_2$, and such low crystallinity may be ascribed to the mild synthetic condition. To further get the structural information of Ni(OH)$_2$, the XRD pattern of Ni(OH)$_2$ with the electrodeposition time extended to 3600 s is displayed in Fig. S5.

Since the interfacial coupling between W$_2$C and Ni(OH)$_2$ can unavoidably trigger the electron interaction, X-ray photoelectron spectroscopy (XPS) was adopted to investigate the surface binding state of obtained samples. The XPS spectra of W$_2$C–Ni(OH)$_2$ together with W$_2$C and Ni(OH)$_2$ are sorted in Fig. 3 for a better comparison, and those of WO$_3$ are displayed in Fig. S4b, c. The survey spectra in Fig. 3b prove the existence of W and C in W$_2$C and the co-existence of W, C, Ni, O in W$_2$C–Ni(OH)$_2$, and such incomplete coverage suggests the shell layer is shaggy, which allows the electrolyte to penetrate through the Ni(OH)$_2$ shell. In the fitted W 4f of W$_2$C (Fig. 3c), the peaks centered at 31.6 eV (W^{5+} 4f$_{7/2}$) and 33.8 eV (W^{5+} 4f$_{5/2}$) can be ascribed to W—C bonds, typical to W$_2$C in general, and the peaks at 35.6 eV (W^{6+} 4f$_{7/2}$) and 37.7 eV (W^{6+} 4f$_{5/2}$) are ascribed to W—O bonds [12,14]. In the fitted Ni 2p (Fig. 3d), the pair peaks of Ni(OH)$_2$ located at 855.5 and 873.1 eV are ascribed to Ni^{2+} 2p$_{3/2}$ and Ni^{2+} 2p$_{1/2}$, coinciding to Ni(OH)$_2$ [37–40].
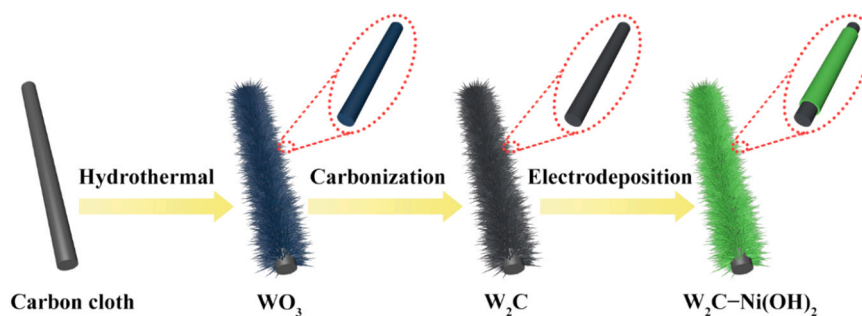
Fig. 1. Schematic representation of the fabrication for W₂C–Ni(OH)₂.

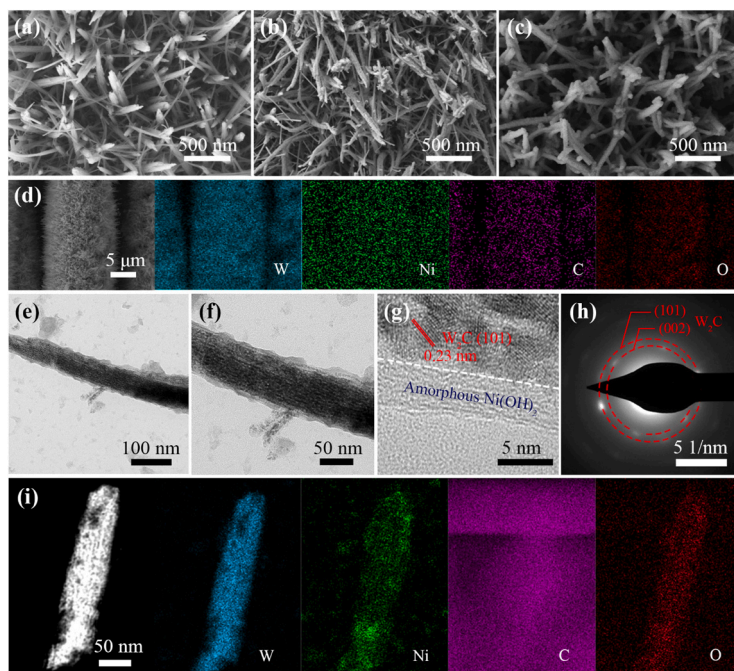**Fig. 2.** SEM images of (a) WO₃, (b) W₂C, and (c) W₂C–Ni(OH)₂. (d) SEM-EDX mapping, (e,f) TEM, (g) HRTEM, (h) the SAED pattern, and (i) STEM-EDX images of W₂C–Ni(OH)₂.
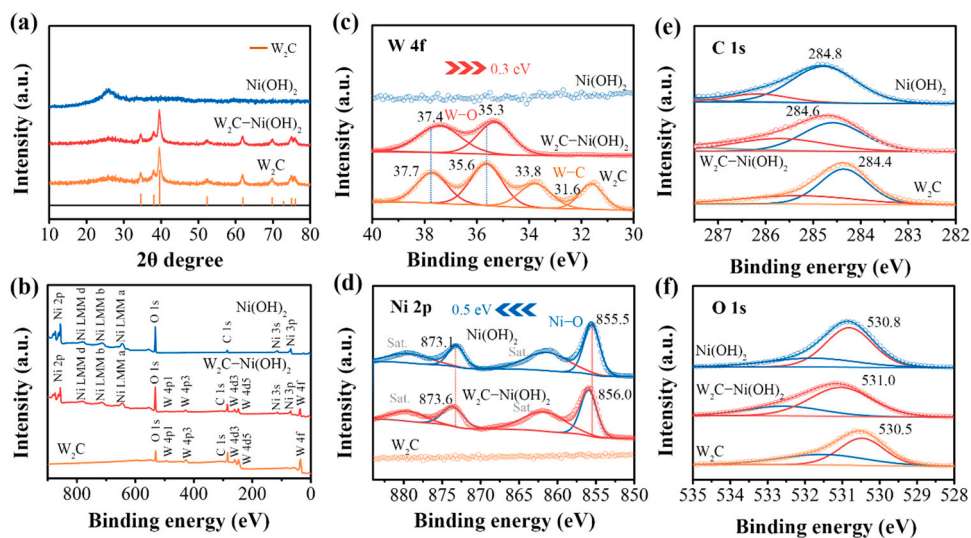

Fig. 3. (a) XRD patterns, (b) XPS survey spectra, high resolution (c) W 4f, (d) Ni 2p, (e) C 1s, and (f) O 1s XPS spectra of W₂C, W₂C–Ni(OH)₂, and Ni(OH)₂.

The doublets observed at higher binding energy are assigned to satellites (identified as "Sat."). After the electrodeposition of W_2C, the W—C signals show a significant decrease and are even undetected. Notably, the W—O peaks shift to lower state with 0.3 eV relative to those of W_2C after the electrodeposition. Meantime, the Ni—O peaks exhibit a positive shift with 0.5 eV, which implies the non-negligible electron interaction between W_2C and $Ni(OH)_2$. Note that C 1s's peak position of metal oxides/carbides may indeed vary [41], thus the measured binding energy values are deconvoluted without calibration. In the C 1s window (Fig. 3e), the C 1s's peak position for W_2C centered at 284.4 eV, and the peak position for $Ni(OH)_2$ centered at 284.6 eV. After the electrodeposition of W_2C, the peak of C 1s shifts towards $Ni(OH)_2$. In the fitted O 1s (Fig. 3f), the peak in $Ni(OH)_2$ at 530.8 eV is assigned to the lattice O [37–40], and the peak at 530.5 eV in W_2C can be associated with W—O bond [42]. Notably, the peak of metal-oxygen reveals a positive shift with 0.2 eV from 530.8 to 531.0 eV, which further indicates the electron redistribution at the interfaces.

3.2. Electrocatalytic properties toward HER

The alkaline HER catalytic performance of obtained samples was evaluated in 1.0 M KOH. Commercial Pt/C coated on CC was also evaluated under the same conditions for comparison. Fig. 4a shows the polarization curves of the obtained samples without *iR*-correction. Among them, the Pt/C exhibits high activity with a low overpotential of 42 mV to reach 10 mA cm^{-2} (η_{10}), whereas it shows a relatively high overpotential of 300 mV to reach the high current density of 100 mA cm^{-2} (η_{100}), which can be ascribed to the limitations such as low mass loading, bulk structure, binder barriers, and sluggish water dissociation kinetics. For the $Ni(OH)_2$ electrode, η_{10} and η_{100} are 439 and 702 mV, respectively, indicating that $Ni(OH)_2$ is inert for HER. For W_2C, η_{10} and η_{100} are 110 and 264 mV, respectively, and such good catalytic activity indicates that the W_2C phase is quite active for HER. Notably, after the incorporation of $Ni(OH)_2$ on W_2C, the η_{10} and η_{100} for W_2C–Ni(OH)$_2$ are reduced to 60 and 213 mV, respectively. The carbonization conditions and loading of $Ni(OH)_2$ were both optimized, as shown in Figs. S6–S8, confirming that W_2C–Ni(OH)$_2$ with a deposition time of 200 s exhibits the best HER performance among all compared samples. The Tafel slopes were derived to elucidate the reaction kinetics during hydrogen release (Fig. 4b, c). The W_2C–Ni(OH)$_2$ electrode exhibited a substantially lower Tafel slope of 55.9 mV dec^{-1} than the bare W_2C (68.8 mV dec^{-1}) or $Ni(OH)_2$ (184.2 mV dec^{-1}), demonstrating an enhanced reaction kinetics of W_2C–Ni(OH)$_2$ during the HER process. The value is even superior to that of commercially available Pt/C

electrode (63.3 mV dec^{-1}). Polarization curves with 90% *iR*-correction show a further improvement of the overpotentials and Tafel slopes (Fig. S9). Additionally, W_2C–Ni(OH)$_2$ exhibits the largest exchange current density (j_0) of 0.863 mA cm^{-2} (Fig. S10). Meanwhile, the electrochemical impedance resistance was conducted to investigate the charge transfer kinetics, and the lowest resistance of W_2C–Ni(OH)$_2$ illustrates a favorable electron transfer process, further demonstrating the optimized HER kinetics (Fig. 4d).

Note that, $Ni(OH)_2$ itself is inert to HER as mentioned above, the greatly reduced values, including the overpotential, Tafel slope, and resistance, after incorporating $Ni(OH)_2$ on W_2C, suggests $Ni(OH)_2$ functions an indispensable role for catalyzing alkaline HER. To further testify the enhanced HER performance, electrochemical double-layer capacitances (C_{dl}) were calculated (Figs. 4e and S11). The C_{dl} value is 179.5 mF cm^{-2} for W_2C–Ni(OH)$_2$, 185.4 mF cm^{-2} for W_2C, and 1.7 mF cm^{-2} for $Ni(OH)_2$. W_2C owns the highest C_{dl} value benefiting from its array structure and high active sites of W_2C, while the lowest C_{dl} value of $Ni(OH)_2$ coincides with its inert HER performance. It is noteworthy that the highly maintained C_{dl} value of W_2C in W_2C–Ni(OH)$_2$ is ascribed to the incomplete coverage, and much smaller value than that in W_2C indicates that the incorporation of $Ni(OH)_2$ hinders the exposure of W_2C, implying that the remarkable performance of W_2C–Ni(OH)$_2$ should not simply be contributed by the high surface area. The corresponding electrochemically active surface area (ECSA) was calculated in Table S1. To further understand the intrinsic activity of each active site, the ECSA-normalized polarization curves were obtained. As expected, the ECSA-normalized current density (J_{ECSA}) for W_2C–Ni(OH)$_2$ is larger than that for W_2C (Fig. S12a). The turnover frequency (TOF) value can reflect closely the activity of each catalytic site of the catalysts, and the calculated TOF values are displayed in Fig. S12b. Apparently, W_2C–Ni(OH)$_2$ shows a higher TOF value, demonstrating more intrinsic active sites for W_2C–Ni(OH)$_2$. The above evidence indicates that W_2C–Ni(OH)$_2$ is much more efficient for catalyzing HER than bare W_2C. Moreover, the performance of the counterpart with similar $Ni(OH)_2$ and W_2C content (denoted as W_2C + Ni(OH)$_2$), in which $Ni(OH)_2$ was loaded on W_2C electrode by the traditional drop-casting method, was assessed (Fig. S13). Although the W_2C + Ni(OH)$_2$ mixture exhibits smaller η_{10} of 95 mV than bare W_2C (η_{10} = 110 mV) and $Ni(OH)_2$ (η_{10} = 439 mV), the activity of the W_2C + Ni(OH)$_2$ mixture is still quite inferior to that of W_2C–Ni(OH)$_2$. Therefore, the core–shell structure is indispensable to the remarkable performance of the W_2C–Ni(OH)$_2$ hybrid. Additionally, the contribution of the crystallinity of $Ni(OH)_2$ to HER performance has been investigated (Fig. S14). After soaking for 8 h with 5 M KOH, the crystalized $Ni(OH)_2$ can be observed in XRD results (Fig. S14a), and the
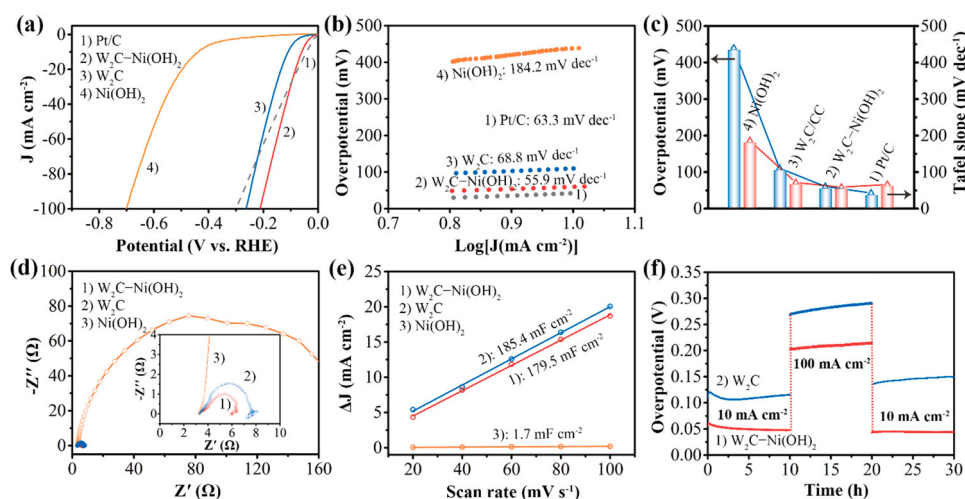

Fig. 4. (a) HER polarization curves, (b) Tafel slopes, (c) comparison of overpotential and Tafel slopes for Pt/C, W_2C–Ni(OH)$_2$, W_2C, and $Ni(OH)_2$. (d) Nyquist plots and (e) the calculated electrochemical double-layer capacitance of W_2C–Ni(OH)$_2$, W_2C, and $Ni(OH)_2$. (f) The multi-current step test for W_2C–Ni(OH)$_2$ and W_2C.

crystalized $Ni(OH)_2$ plays a positive role in the promoted HER performance of W_2C–$Ni(OH)_2$ (Fig. S14b). Impressively, Tables S2 and S3 show the remarkable activities of W_2C–$Ni(OH)_2$ compared with the previously representative W_2C-based catalysts and dual-site catalysts for alkaline HER.

Importantly, chronic durability has also been considered as a pivotal criterion for evaluating tungsten carbide-based catalysts, especially in such strongly alkaline media. The multi-current stability tests for W_2C and W_2C–$Ni(OH)_2$ were performed (Fig. 4f). For W_2C–$Ni(OH)_2$, the needed overpotential decreases firstly and stabilizes at around 48 mV in the initial 10 mA cm^{-2}, and even keeps steady (only a slight increase) at 100 mA cm^{-2}. In the final 10 mA cm^{-2}, the overpotential keeps steady at 44 mV, confirming the excellent durability of W_2C–$Ni(OH)_2$. For W_2C, overpotentials of each current density show a slight increment as HER proceeds, and an obvious increment (about 20 mV) can be observed between the initial and final step of 10 mA cm^{-2}, indicating the undesirable long-term durability of W_2C in alkaline media. To get further insights into the structure-performance relationship of W_2C and W_2C–$Ni(OH)_2$, XRD measurements after HER were carried out to detect the crystalline changes (Fig. S15). The peak intensity of W_2C shows a sharp decrease, which is ascribed to the inevitable corrosive loss of partial W_2C in such strong alkaline media. To more convincingly testify the protective role of the $Ni(OH)_2$ shell, long-term stability tests at 50 mA cm^{-2} for 30 h were conducted (Fig. S16), and the inductively coupled plasma-optical emission spectroscopy (ICP-OES) was employed to quantify the content of W leached from the catalysts into the electrolyte (Table S4). The smaller W loss of W_2C–$Ni(OH)_2$ than that of bare W_2C indicates that the $Ni(OH)_2$ shell, to a certain extent, serves as a positive role in alleviating the corrosive loss of the core W_2C during HER. The SEM images after HER manifest the well-maintained morphology of W_2C–$Ni(OH)_2$ (Fig. S17). The TEM images of W_2C–$Ni(OH)_2$ after HER verify that the core-shell structure and the crystalline phase of W_2C are well maintained (Fig. S18). The XPS spectra show the surface component changes of W_2C–$Ni(OH)_2$ and W_2C after HER (Figs. S19 and S20). Notably, the peaks of W_2C after HER in Fig. S20a also exhibit a negative shift of about 0.4 eV, similar to that of W_2C–$Ni(OH)_2$ in Fig. 3c. And the results above

suggest that the negative shift of the peaks in W 4f can be triggered by reductive electrochemical activation. Particularly, W_2C–$Ni(OH)_2$ after HER even shows higher bonding state of W 4f in contrast to W_2C after HER (Fig. S21).

3.3. Theoretical mechanism discussion

To understand the electronic interaction that occurred at the W_2C–$Ni(OH)_2$ interface theoretically, the isosurfaces of charge density difference were calculated (Fig. 5a). At the interfacial region, substantial charges accumulate, indicating that such interfacial interaction results in a strong electron redistribution. To get further insights into the electron transfer behavior of the hybrid structure, the Bader charge analysis was conducted to quantitatively analyze the electron gain and loss (Fig. 5b). The Bader charge for W increases from 0.56 to 0.68 (W_2C to W_2C–$Ni(OH)_2$), meanwhile, the charge number of Ni increases from 0.65 to 0.71 ($Ni(OH)_2$ to W_2C–$Ni(OH)_2$), indicating the electron depletion at both W and Ni region. Notably, for H, the shift from 0.30 to −0.19 ($Ni(OH)_2$ to W_2C–$Ni(OH)_2$) indicates that the electron mainly accumulates at the H region. Therefore, despite the charge transfer from W_2C to the $Ni(OH)_2$ as demonstrated by charge density difference, further Bader charge analysis indicates that both Ni and W regions are positively charged, which matches well with the XPS results shown in Figs. 3d and S21. The above results indeed demonstrate the strong electronic interaction at interfaces.

To provide a more comprehensive testification of the promoted HER process of W_2C–$Ni(OH)_2$, DFT calculations are conducted to investigate the main reaction steps on the catalyst surface. We construct the (101) slab structure of W_2C and take the metal atom as the active site for HER. The atomic positions of the surface models were optimized by DFT calculation to achieve a stable structure (Fig. S22a). The DFT optimized structures for W_2C–$Ni(OH)_2$ are displayed in Fig. S22b. For the alkaline HER reaction process, two steps have been proposed including the Volmer reaction ($H_2O + e^- \rightarrow H_{ad} + OH^-$); Tafel reaction ($H^* + H^* \rightarrow H_2$), or Heyrovsky reaction ($H^* + H_2O + e^- \rightarrow H_2 + OH^-$). Prior to water dissociation, it is a consensus that the adsorption energy of H_2O

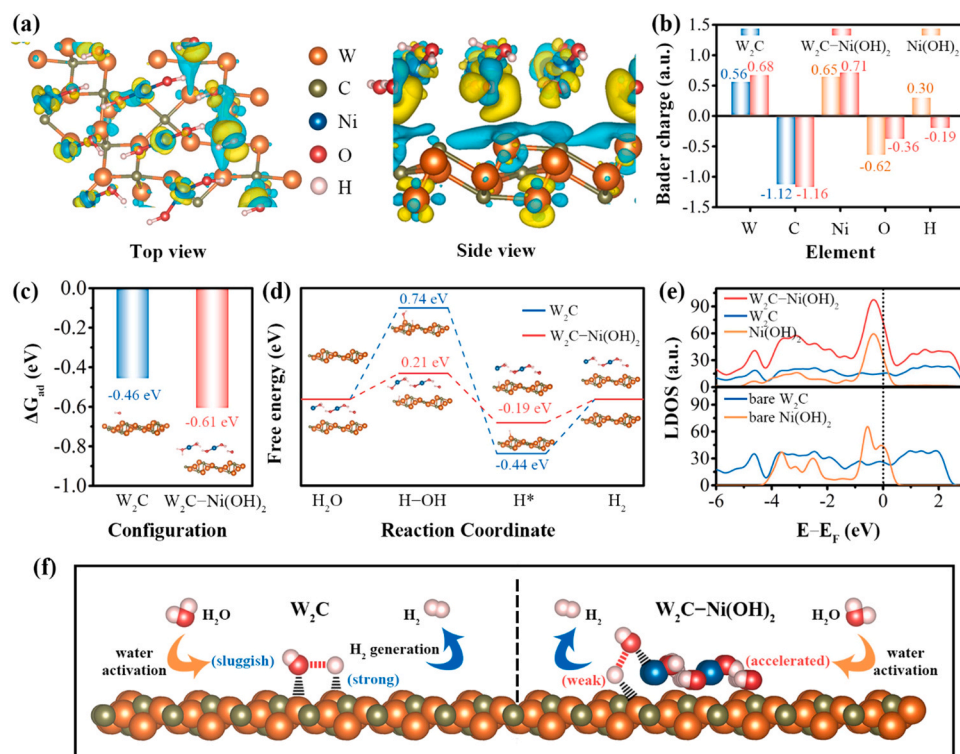**Fig. 5.** (a) Charge distribution at the W_2C–$Ni(OH)_2$ interface with the isovalue of 0.003 e$^-$ per Bohr; the yellow and cyan represent negative charges and positive charges, respectively. (b) Average Bader charge of W, C, Ni, O, and H in optimized supercell geometry for W_2C–$Ni(OH)_2$, $Ni(OH)_2$, and W_2C. (c) Calculated water adsorption energy (ΔG_{H2O^*}) and (d) free energy diagram on W_2C and W_2C–$Ni(OH)_2$. (e) Local density of states (LDOS) of W_2C, $Ni(OH)_2$, and W_2C–$Ni(OH)_2$ with aligned Fermi level. (f) Schematic illustration of alkaline HER on W_2C (left) and W_2C–$Ni(OH)_2$ (right), respectively.

(ΔG_{H2O^*}) plays an important role for alkaline HER. The ΔG_{H2O^*} for W$_2$C–Ni(OH)$_2$ based on two cases was calculated and the interfacial edge region showed stronger binding energy (Fig. S23) [43]. Notably, W$_2$C–Ni(OH)$_2$ displays much negative adsorption energy (−0.61 eV) than the bare W$_2$C (−0.46 eV), suggesting that the W$_2$C–Ni(OH)$_2$ hybrid structure is more favorable for the adsorption and activation of H$_2$O, which provides support for the subsequent water dissociation (Fig. 5c). Such enhanced interfacial reactivity correlates heavily with the strong electronic interaction at the interfaces [44]. Fig. 5d shows the energy differences diagram of the main reaction pathway for alkaline HER. For the dissociation of H$_2$O, the bare W$_2$C catalyst displays an energy barrier (ΔG_{H2O}) of up to 0.74 eV, while the W$_2$C–Ni(OH)$_2$ hybrid structure shows a quite reduced value of ΔG_{H2O} (0.21 eV), indicating that the H—OH bonds are more effortlessly broken down on the hybrid surface. These results demonstrate a positive role for boosting the water adsorption and dissociation and thus the sluggish Volmer step can be substantially accelerated. Another activity descriptor (ΔG_{H^*}) has been applied to evaluate the HER performance, where (ΔG_{H^*}) close to zero represents a suitable HER catalyst [5,45]. As shown in Fig. 5d, the ΔG_{H^*} are −0.44 and −0.19 eV for W$_2$C (two sites were explored, see Fig. S24) and W$_2$C–Ni(OH)$_2$ hybrid, respectively, indicating that the interfacial interaction endows the hybrid catalyst with a positive effect on hydrogen desorption. In this way, the subsequent H$_2$ production on W$_2$C–Ni(OH)$_2$ can also be promoted. Therefore, the synergistic effect can be achieved at the W$_2$C–Ni(OH)$_2$ interface, which result in favorable hydroxyl and hydrogen species energetics, thus accelerating the whole reaction process. In general, the calculated results agree well with the experimental results. Moreover, the advantage of the W$_2$C–Ni(OH)$_2$ hybrid is also verified by comparing the local density of states (LDOS) as shown in Fig. 5e. Compared with those of the bare W$_2$C and bare Ni(OH)$_2$ surface, the LDOS of W$_2$C–Ni(OH)$_2$ exhibits a much higher intensity, and near the Fermi level, it is populated both by the W$_2$C and Ni(OH)$_2$ constituents, which reveals the modulated electronic structure and the introduction of Ni(OH)$_2$ can provide more catalytic sites and cooperate with W$_2$C to catalyze HER reaction [46–48]. Combining all the experimental results with the calculation results, the alkaline HER mechanism for W$_2$C–Ni(OH)$_2$ is displayed in Fig. 5f. During Volmer step, adsorbed H$_2$O at the interface can be effortlessly split up to create H* and OH$^-$ on Ni(OH)$_2$ sites. Then the newly formed H* species are subsequently captured by W$_2$C sites and thus react to produce H$_2$ through the Tafel or Heyrovsky steps. Benefiting from the positive roles of Ni(OH)$_2$, both hydrogen desorption and water dissociation steps are accelerated. In contrast, both water dissociation and hydrogen desorption are limited to the bare W$_2$C surface, resulting in slower kinetics and lower activity.

3.4. Electrocatalytic properties toward full water electrolysis

Considering that Ni(OH)$_2$ is an active component for oxygen evolution reaction (OER), meanwhile, the utilization of W$_2$C for OER has not been reported, the alkaline OER catalytic performance of those electrodes was next tested. As displayed in Fig. 6a, W$_2$C–Ni(OH)$_2$ possesses much lower η_{10} of 278 mV than the counterparts made from Ni(OH)$_2$ (η_{10} = 331 mV) and W$_2$C (η_{10} = 416 mV). Moreover, W$_2$C–Ni(OH)$_2$ manifested an impressively low Tafel slope of 51.7 mV dec^{-1}, which is substantially better than that for Ni(OH)$_2$ and W$_2$C electrodes (Fig. 6b). Note that the OER performance of W$_2$C is much inferior to that of Ni(OH)$_2$, thus in W$_2$C–Ni(OH)$_2$, the real active component for OER should be Ni(OH)$_2$ [49], while the W$_2$C wires array serves the conductive substrate for continuous electron transport and provides abundant locations for Ni(OH)$_2$ loading. Encouraged by the extraordinary HER and OER performance of W$_2$C–Ni(OH)$_2$, the alkaline electrolyzer assembled with W$_2$C–Ni(OH)$_2$ shows a relatively small driving voltage (about 1.47 V), which substantially exceeds that assembled with bare W$_2$C. Furthermore, it delivers small voltages of 1.55 and 1.73 V to afford 10 and 50 mA cm^{-2} (Fig. 6c), respectively, and can steadily operate for 30 h (Fig. 6d). To correlate the electrochemical results with the actual production rates of H$_2$ and O$_2$ and to evaluate the faradaic efficiency, the amount of gas produced by the experiment was quantified through the water drainage method (Fig. S25). The evolved gas amount matches well with the theoretical amount when water electrolysis proceeds for 2 h, indicating that the Faraday efficiency for HER and OER is nearly 100%, demonstrating that the current in both cathode and anode was mainly attributed to water splitting.

4. Conclusion

In summary, we have constructed an interfacial engineered W$_2$C–Ni(OH)$_2$ catalyst, which has remarkable catalytic performance for alkaline HER. Experimental evidence combined with DFT calculations reveals that the strong interfacial interaction occurs between the host W$_2$C and the guest Ni(OH)$_2$ components, which was beneficial to the optimization

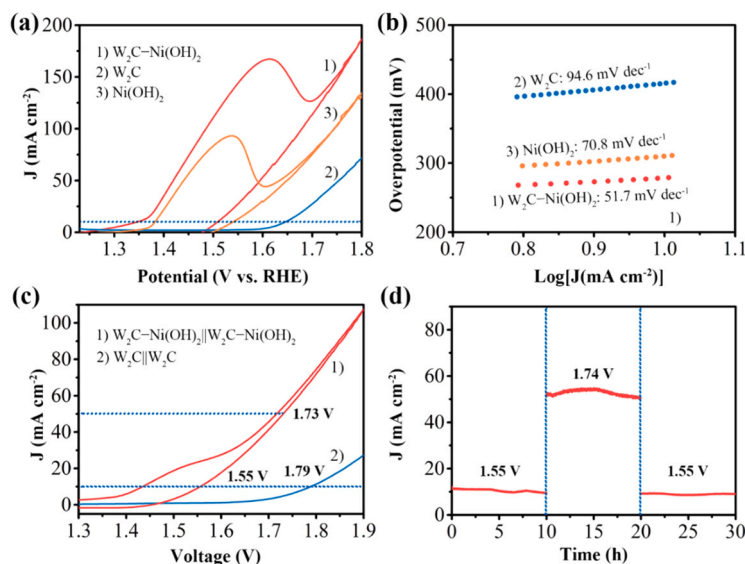**Fig. 6.** (a) CV curves and (b) the corresponding Tafel slopes (backward scan) of the W$_2$C–Ni(OH)$_2$, W$_2$C, and Ni(OH)$_2$ electrodes at a scan rate of 5 mV s^{-1}. (c) CV curves of the W$_2$C–Ni(OH)$_2$||W$_2$C–Ni(OH)$_2$ and W$_2$C||W$_2$C for full water electrolysis at a scan rate of 5 mV s^{-1}. (d) The multi-current step stability test of the W$_2$C–Ni(OH)$_2$||W$_2$C–Ni(OH)$_2$.

of the interfacial reactivity with favorable hydroxyl and hydrogen species energetics, and verifies a crossing point of HBE theory and bifunctional mechanism in the hybrid catalyst for the promoted performance. The incorporation of $Ni(OH)_2$ promotes H_2O adsorption at the interfacial region and provides additional locations for water dissociation, which greatly improves the rate-limiting Volmer step of the hybrid catalyst. Meantime, it also alleviates the bonding strength of H* intermediate at W_2C site, thus promoting the subsequent association to form H_2. Our work provides a feasible pathway for constructing other carbides for efficient alkaline HER catalysis.

CRediT authorship contribution statement

Hong Chuan Fu: Conceptualization, Investigation, Writing – original draft. **Xiao Hu Wang:** Visualization, Investigation, Resources. **Xiao Hui Chen:** Data curation, Software. **Qing Zhang:** Validation, Software. **Nian Bing Li:** Supervision, Funding acquisition, Writing – review & editing. **Hong Qun Luo:** Supervision, Funding acquisition, Writing – review & editing.

Declaration of Competing Interest

The authors declare that they have no known competing financial interests or personal relationships that could have appeared to influence the work reported in this paper.

Acknowledgments

Appendix A. Supplementary material

Supplementary data associated with this article can be found in the online version at doi:10.1016/j.apcatb.2021.120818.

References

[1] J.A. Turner, Sustainable hydrogen production, Science 305 (2004) 972–974.
[2] X. Zou, Y. Zhang, Noble metal-free hydrogen evolution catalysts for water splitting, Chem. Soc. Rev. 44 (2015) 5148–5180.
[3] J.D. Holladay, J. Hu, D.L. King, Y. Wang, An overview of hydrogen production technologies, Catal. Today 139 (2009) 244–260.
[4] J. Wang, F. Xu, H. Jin, Y. Chen, Y. Wang, Non-noble metal-based carbon composites in hydrogen evolution reaction: fundamentals to applications, Adv. Mater. 29 (2017), 1605838.
[5] Y. Zheng, Y. Jiao, Y. Zhu, L.H. Li, Y. Han, Y. Chen, M. Jaroniec, S.-Z. Qiao, High electrocatalytic hydrogen evolution activity of an anomalous ruthenium catalyst, J. Am. Chem. Soc. 138 (2016) 16174–16181.
[6] L. Wang, C. Lin, D. Huang, J. Chen, L. Jiang, M. Wang, L. Chi, L. Shi, J. Jin, Optimizing the Volmer step by single-layer nickel hydroxide nanosheets in hydrogen evolution reaction of platinum, ACS Catal. 5 (2015) 3801–3806.
[7] R. Subbaraman, D. Tripkovic, D. Strmcnik, K.-C. Chang, M. Uchimura, A. P. Paulikas, V. Stamenkovic, N.M. Markovic, Enhancing hydrogen evolution activity in water splitting by tailoring Li^+-Ni $(OH)_2$-Pt interfaces, Science 334 (2011) 1256–1260.
[8] T. Liu, D. Liu, F. Qu, D. Wang, L. Zhang, R. Ge, S. Hao, Y. Ma, G. Du, A.M. Asiri, Enhanced electrocatalysis for energy-efficient hydrogen production over CoP catalyst with nonelectroactive Zn as a promoter, Adv. Energy Mater. 7 (2017), 1700020.
[9] Y.-R. Zheng, P. Wu, M.-R. Gao, X.-L. Zhang, F.-Y. Gao, H.-X. Ju, R. Wu, Q. Gao, R. You, W.-X. Huang, Doping-induced structural phase transition in cobalt diselenide enables enhanced hydrogen evolution catalysis, Nat. Commun. 9 (2018) 1–9.
[10] Q. Gao, W. Zhang, Z. Shi, L. Yang, Y. Tang, Structural design and electronic modulation of transition-metal-carbide electrocatalysts toward efficient hydrogen evolution, Adv. Mater. 31 (2019), 1802880.
[11] J.G. Chen, Carbide and nitride overlayers on early transition metal surfaces: preparation, characterization, and reactivities, Chem. Rev. 96 (1996) 1477–1498.
[12] Q. Gong, Y. Wang, Q. Hu, J. Zhou, R. Feng, P.N. Duchesne, P. Zhang, F. Chen, N. Han, Y. Li, Ultrasmall and phase-pure W_2C nanoparticles for efficient electrocatalytic and photoelectrochemical evolution, Nat. Commun. 7 (2016) 1–8.
[13] F. Wang, P. He, Y. Li, T.A. Shifa, Y. Deng, K. Liu, Q. Wang, F. Wang, Y. Wen, Z. Wang, Interface engineered $W_xC@WS_2$ nanostructure for enhanced hydrogen evolution catalysis, Adv. Funct. Mater. 27 (2017), 1605802.
[14] Z. Chen, W. Gong, S. Cong, Z. Wang, G. Song, T. Pan, X. Tang, J. Chen, W. Lu, Z. Zhao, Eutectoid-structured WC/W_2C heterostructures: a new platform for long-term alkaline hydrogen evolution reaction at low overpotentials, Nano Energy 68 (2019), 104335.
[15] W.F. Chen, J.M. Schneider, K. Sasaki, C.H. Wang, J. Schneider, S. Iyer, S. Iyer, Y. Zhu, J.T. Muckerman, E. Fujita, Tungsten carbide–nitride on graphene nanoplatelets as a durable hydrogen evolution electrocatalyst, ChemSusChem 7 (2014) 2414–2418.
[16] L.-N. Zhang, Y.-Y. Ma, Z.-L. Lang, Y.-H. Wang, S.U. Khan, G. Yan, H.-Q. Tan, H.-Y. Zang, Y.-G. Li, Ultrafine cable-like WC/W_2C heterojunction nanowires covered by graphitic carbon towards highly efficient electrocatalytic hydrogen evolution, J. Mater. Chem. A 6 (2018) 15395–15403.
[17] Z. Kou, T. Wang, H. Wu, L. Zheng, S. Mu, Z. Pan, Z. Lyu, W. Zang, S.J. Pennycook, J. Wang, Twinned tungsten carbonitride nanocrystals boost hydrogen evolution activity and stability, Small 15 (2019), 1900248.
[18] G. Yan, C. Wu, H. Tan, X. Feng, L. Yan, H. Zang, Y. Li, N-Carbon coated $P-W_2C$ composite as efficient electrocatalyst for hydrogen evolution reactions over the whole pH range, J. Mater. Chem. A 5 (2017) 765–772.
[19] M.B. Zellner, J.G.G. Chen, Surface science and electrochemical studies of WC and W_2C PVD films as potential electrocatalysts, Catal. Today 99 (2005) 299–307.
[20] D.J. Ham, J.S. Lee, Transition metal carbides and nitrides as electrode materials for low temperature fuel cells, Energies 2 (2009) 873–899.
[21] X. Yuan, W. Huang, L. Kong, S. Guo, Y. Cheng, Ditungsten carbide nanoparticles homogeneously embedded in carbon nanofibers for efficient hydrogen production, Chem. Eng. J. 420 (2021), 130480.
[22] M. Miles, M. Thomason, Periodic variations of overvoltages for water electrolysis in acid solutions from cyclic voltammetric studies, J. Electrochem. Soc. 123 (1976) 1459–1461.
[23] J.K. Nørskov, T. Bligaard, A. Logadottir, J. Kitchin, J.G. Chen, S. Pandelov, U. Stimming, Trends in the exchange current for hydrogen evolution, J. Electrochem. Soc. 152 (2005) J23.
[24] J. Zheng, W. Sheng, Z. Zhuang, B. Xu, Y. Yan, Universal dependence of hydrogen oxidation and evolution reaction activity of platinum-group metals on pH and hydrogen binding energy, Sci. Adv. 2 (2016), e1501602.
[25] W. Sheng, M. Myint, J.G. Chen, Y. Yan, Correlating the hydrogen evolution reaction activity in alkaline electrolytes with the hydrogen binding energy on monometallic surfaces, Energy Environ. Sci. 6 (2013) 1509–1512.
[26] I. Ledezma-Yanez, W.D.Z. Wallace, P. Sebastián-Pascual, V. Climent, J.M. Feliu, M. T. Koper, Interfacial water reorganization as a pH-dependent descriptor of the hydrogen evolution rate on platinum electrodes, Nat. Energy 2 (2017) 1–7.
[27] E. Liu, J. Li, L. Jiao, H.T.T. Doan, Z. Liu, Z. Zhao, Y. Huang, K. Abraham, S. Mukerjee, Q. Jia, Unifying the hydrogen evolution and oxidation reactions kinetics in base by identifying the catalytic roles of hydroxyl-water-cation adducts, J. Am. Chem. Soc. 141 (2019) 3232–3239.
[28] R. Subbaraman, D. Tripkovic, K.-C. Chang, D. Strmcnik, A.P. Paulikas, P. Hirunsit, M. Chan, J. Greeley, V. Stamenkovic, N.M. Markovic, Trends in activity for the water electrolyser reactions on 3d M (Ni, Co, Fe, Mn) hydr (oxy) oxide catalysts, Nat. Mater. 11 (2012) 550–557.
[29] J. Guan, C. Li, J. Zhao, Y. Yang, W. Zhou, Y. Wang, G.-R. Li, FeOOH-enhanced bifunctionality in Ni_3N nanotube arrays for water splitting, Appl. Catal. B Environ. 269 (2020), 118600.
[30] B. Zhang, J. Liu, J. Wang, Y. Ruan, X. Ji, K. Xu, C. Chen, H. Wan, L. Miao, J. Jiang, Interface engineering: the $Ni(OH)_2/MoS_2$ heterostructure for highly efficient alkaline hydrogen evolution, Nano Energy 37 (2017) 74–80.
[31] N. Zhang, C. Wang, F. Zhao, K. Han, Y. Ma, Y. Li, J. Liu, Self-healing γ-FeOOH decorated onto MoS_2 nanosheets for boosting the hydrogen evolution in alkaline media, Appl. Catal. B Environ. 297 (2021), 120456.
[32] C. Lv, X. Wang, L. Gao, A. Wang, S. Wang, R. Wang, X. Ning, Y. Li, D. W. Boukhvalov, Z. Huang, Triple functions of $Ni(OH)_2$ on the surface of WN nanowires remarkably promoting electrocatalytic activity in full water splitting, ACS Catal. 10 (2020) 13323–13333.
[33] X. Yu, J. Zhao, M. Johnsson, Interfacial engineering of nickel hydroxide on cobalt phosphide for alkaline water electrocatalysis, Adv. Funct. Mater. 31 (2021), 2101578.
[34] Q. Zhang, W. Xiao, W.H. Guo, Y.X. Yang, J.L. Lei, H.Q. Luo, N.B. Li, Macroporous array induced multiscale modulation at the surface/interface of $Co(OH)_2/NiMo$ self-supporting electrode for effective overall water splitting, Adv. Funct. Mater. 31 (2021), 2102117.
[35] K. Xu, H. Ding, M. Zhang, M. Chen, Z. Hao, L. Zhang, C. Wu, Y. Xie, Regulating water-reduction kinetics in cobalt phosphide for enhancing HER catalytic activity in alkaline solution, Adv. Mater. 29 (2017), 1606980.
[36] Z. Xing, D. Wang, Q. Li, A.M. Asiri, X. Sun, Self-standing Ni-WN heterostructure nanowires array: a highly efficient catalytic cathode for hydrogen evolution reaction in alkaline solution, Electrochim. Acta 210 (2016) 729–733.
[37] Z. Dong, Z. Lin, Y. Yao, L. Jiao, Crystalline $Ni(OH)_2$/amorphous $NiMoO_x$ mixed-catalyst with Pt-like performance for hydrogen production, Adv. Energy Mater. 9 (2019), 1902703.
[38] Q. Xu, H. Jiang, H. Zhang, Y. Hu, C. Li, Heterogeneous interface engineered atomic configuration on ultrathin $Ni(OH)_2/Ni_3S_2$ nanoforests for efficient water splitting, Appl. Catal. B Environ. 242 (2019) 60–66.
[39] D. Kim, J. Park, J. Lee, Z. Zhang, K. Yong, $Ni(OH)_2$-WP hybrid nanorod arrays for highly efficient and durable hydrogen evolution reactions in alkaline media, ChemSusChem 11 (2018) 3618–3624.

[40] L. Zhang, I.S. Amiinu, X. Ren, Z. Liu, G. Du, A.M. Asiri, B. Zheng, X. Sun, Surface modification of a NiS_2 nanoarray with $Ni(OH)_2$ toward superior water reduction electrocatalysis in alkaline media, Inorg. Chem. 56 (2017) 13651–13654.

[41] G. Greczynski, L. Hultman, Compromising science by ignorant instrument calibration—need to revisit half a century of published XPS data, Angew. Chem. Int. Ed. 59 (2020) 5002–5006.

[42] B. Zhang, J. Hou, Y. Wu, S. Cao, Z. Li, X. Nie, Z. Gao, L. Sun, Tailoring active sites in mesoporous defect-rich NC/V_0-WON heterostructure array for superior electrocatalytic hydrogen evolution, Adv. Energy Mater. 9 (2019), 1803693.

[43] X. Wang, Y. Zheng, W. Sheng, Z.J. Xu, M. Jaroniec, S.-Z. Qiao, Strategies for design of electrocatalysts for hydrogen evolution under alkaline conditions, Mater. Today 36 (2020) 125–138.

[44] Y. Liu, Q. Li, R. Si, G.-D. Li, W. Li, D.-P. Liu, D. Wang, L. Sun, Y. Zhang, X. Zou, Coupling sub-nanometric copper clusters with quasi-amorphous cobalt sulfide yields efficient and robust electrocatalysts for water splitting reaction, Adv. Mater. 29 (2017), 1606200.

[45] Y. Guo, L. Gan, C. Shang, E. Wang, J. Wang, A cake-style $CoS_2@MoS_2$/RGO hybrid catalyst for efficient hydrogen evolution, Adv. Funct. Mater. 27 (2017), 1602699.

[46] X. Yu, J. Zhao, L.-R. Zheng, Y. Tong, M. Zhang, G. Xu, C. Li, J. Ma, G. Shi, Hydrogen evolution reaction in alkaline media: alpha-or beta-nickel hydroxide on the surface of platinum? ACS Energy Lett. 3 (2017) 237–244.

[47] Y. Wang, E. Song, W. Qiu, X. Zhao, Y. Zhou, J. Liu, W. Zhang, Recent progress in theoretical and computational investigations of structural stability and activity of single-atom electrocatalysts, Prog. Nat. Sci. Mater. Int. 29 (2019) 256–264.

[48] J. Zhang, Y. Zhao, X. Guo, C. Chen, C.-L. Dong, R.-S. Liu, C.-P. Han, Y. Li, Y. Gogotsi, G. Wang, Single platinum atoms immobilized on an MXene as an efficient catalyst for the hydrogen evolution reaction, Nat. Catal. 1 (2018) 985–992.

[49] X. Lu, C. Zhao, Electrodeposition of hierarchically structured three-dimensional nickel-iron electrodes for efficient oxygen evolution at high current densities, Nat. Commun. 6 (2015) 1–7.